Article:
Kuttippurath, J, Ardra, D, Raj, S et al. (2023) A seasonal OH minimum region over the Indian Ocean? Atmospheric Environment, 295. 119536. ISSN: 1352-2310

https://doi.org/10.1016/j.atmosenv.2022.119536

A seasonal OH minimum region over the Indian Ocean?

J. Kuttippurath[1*], D. Ardra[1], S. Raj[1] and W. Feng[2,3]

[1] CORAL, Indian Institute of Technology Kharagpur, Kharagpur–721302, India.

[2] National Centre for Atmospheric Science, University of Leeds, Leeds, LS2 9PH, UK

[3] School of Earth and Environment, University of Leeds, Leeds, LS2 9JT, UK

*Correspondence: J. Kuttippurath (jayan@coral.iitkgp.ac.in)

ADDRESS FOR COMMUNICATIONS

Prof. Jayanarayanan Kuttippurath

CORAL, Indian Institute of Technology Kharagpur,

721302 Kharagpur, West Bengal, India

Phone: 0091 9475472847

Email: jayan@coral.iitkgp.ac.in

HIGHLIGHTS

- There exists a seasonal OH minimum region over Indian Ocean in spring
- A secondary minimum in autumn, but values are slightly higher than that in spring
- SO_2, CO, O_3 and H_2O chemistry play a key role in the observed minimum in the region
- The OH minimum can affect the air quality in the Indian Ocean region

ABSTRACT

As the hydroxyl radical (OH) is the cleansing agent of the atmosphere, reduction in its concentration is a great concern for air quality and transport of trace gases across the latitudes and altitudes. In addition, OH determines the lifetime of most trace gases and non-CO_2 greenhouse gases in the atmosphere. Since many pollutants have adverse health effects and are greenhouse gases, the changes in OH concentrations directly or indirectly affect public health and climate. Our analysis with OH data (from Tropospheric Emission Spectrometer and Copernicus Atmosphere Monitoring Service reanalyses) for the past 14 (2005–2018) years finds an OH minimum region over Indian Ocean, in the eastern Bay of Bengal at 6°–14°N and 92°–95°E. The Indian Ocean OH minimum reaches to 15×10^4 molec.cm^{-3} in April, and a secondary minimum of 18×10^4 molec.cm^{-3} in September–November. This seasonal minimum found around the Andaman and Nicobar Islands also hosts an active volcano, which releases noticeable amount of SO_2 (OH sink) throughout the year. In addition, the biomass burning in spring and thus, the distribution of CO has a profound influence on the OH distribution in this region as Southeast Asia is one of the global hotspots of biomass burning, and the Indian Ocean OH minimum is located near that region. The El Niño and La Niño events also control the tropospheric ozone and CO distribution, and thus the interannual variability of OH minimum there. The WACCM model simulations reproduce the general latitudinal distribution and average seasonal cycle of OH, but not the extreme minimum OH values, although the simulations show the annual minimum in winter (December–January) in both ocean regions, which demands dedicated studies using chemical transport models. Therefore, this study reveals a seasonal OH minimum over Indian Ocean, which is very likely to influence the regional air quality and trace gas transport in the tropics.

Short title: Indian Ocean OH minimum

Key words: Indian Ocean; Stratosphere; troposphere; Pollution; western Pacific Ocean; OH

1. Introduction

Hydroxyl (OH) is a short-lived (less than a second) free radical and the most effective scavenger in the troposphere. It is the major oxidant in the lower troposphere that determines the lifetime of most trace gases and greenhouse gases (GHGs) such as methane (CH_4) in the atmosphere (Lelieveld et al., 2016; Nicely et al., 2018), and therefore, is a climate relevant gas. OH radical is called the "detergent of atmosphere" due to its role and ability to clean the atmosphere. The general composition of stratosphere is influenced by the species that are transported from the troposphere. Hydroxyl radicals in the troposphere react with some short-lived species and convert them into soluble products. Therefore, OH radicals in the troposphere mask the stratosphere from many tropospheric emissions (Rex et al., 2014). The variability of OH in the troposphere is key not just for the supply of chemical species such as SO_2 and CH_4 to the stratosphere, but also for the atmospheric lifetime of several trace gases (Manning et al., 2005).

There are multitude of sources and sinks for the hydroxyl radical. The primary production of OH is by the photodissociation of ozone by ultraviolet (UV) sunlight with a wavelength of the photon (hv) shorter than 330 nm in the presence of water vapor (Levy, 1971):

$O_3 + h\nu\ (\lambda < 330\ nm) \rightarrow O(^1D) + O_2$ (R 1)

$O(^1D) + H_2O \rightarrow 2OH$ (R 2)

Recently, it is found that this source has a relatively small contribution compared to other sources under polluted conditions (e.g. Elshorbany et al., 2010; Vogel et al., 2003). Photolysis of HCHO is a daytime source of HO_2 radicals:

$HCHO + hv\ (threshold, \lambda < 338\ nm) \rightarrow H + HCO$ (R 3)

$H + O_2 + M \rightarrow HO_2 + M$ (R 4)

$HCO + O_2 \rightarrow HO_2 + CO$ (R 5)

The conversion of HO_2 to OH depends on the availability of NO.

120 $HO_2 + NO \rightarrow OH + NO_2$ (R 6)

121 The OH radical is also formed by the ozonolysis of alkenes. In addition, nitrous acid (HONO) contributes to
122 the formation of OH radical:

123 HONO + hv (threshold, $\lambda < 400$ nm) $\rightarrow$ OH + NO (R 7)

124 This is a major source of daytime OH concentration (Elshorbany et al., 2010). The OH radical reacts with
125 reduced and partly oxidised gases such as CH_4, CO and non-methane Volatile Organic Compounds
126 (NMVOC). CO and CH_4 are the direct sinks of atmospheric OH (Lu et al., 1993).

127 $CO + OH \rightarrow CO_2 + H$ (R 8)

128 $CH_4 + OH \rightarrow CH_3 + H_2O$ (R 9)

129 Also, under high NO_x conditions, permanent loss processes are dominated by the reaction of OH with NO_2.

130 $OH + NO_2 (M) \rightarrow HNO_3 (M)$ (R 10)

131 Therefore, the regional variability of OH depends on several factors.

132

133 An OH minimum has been found in the tropical western Pacific centered at 17° N /158° E. This "OH hole"
134 was reported based on the observations of very small values of tropospheric O_3 in this region (Rex et al.,
135 2014). The explanation for this is that suppression of primary OH production due to low O_3 or deficiency of
136 secondary production due to low NO (Wolfe et al., 2019a,b). It implies that the region has very low
137 atmospheric pollution or pristine air. Here, we examine whether there is any OH minimum zone over other
138 ocean basins, e.g. Indian Ocean. Our analyses expose an OH minimum (at the surface level) over Indian
139 Ocean at around 12° N/93° E. Therefore, we present a detailed assessment of the spatio-temporal
140 variability of this OH minimum for the past 14 years (2005–2018) using the TES (Tropospheric Emission
141 Spectrometer) reanalysis data. Since the analysis and identification of a minimum value is very sensitive
142 and could be also data specific, we have used another reanalysis data, the Copernicus Atmosphere
143 Monitoring Service (CAMS). Furthermore, we have also used a global chemical transport model (CTM) for

144 the simulation of OH in both oceanic regions for examining the representation of OH minimum in the state-
145 of-the-art CTMs. The distribution of OH is compared to that of CO, CH_4, HCHO, SO_2, H_2O, NO_x, HNO_3 and O_3
146 in the minimum region. Note that there are no measurements available in this region, and therefore, we
147 have used the reanalysed data and model simulations. The influence of meteorological and oceanic factors
148 such as clouds, water vapour, precipitation, winds and sea surface temperature (SST) on the variability of
149 OH is also discussed. The OH minimum over this region is compared to that in the tropical western Pacific
150 and reasons for these minima are assessed.
151
152 ## 2. Data and Methods
153 The TES chemical reanalysis data have a horizontal resolution of 1.1°×1.1° (e.g. Cady-Pereira et al., 2017;
154 Miyazaki and Bowman, 2017). Chemical reanalysis is a technique in which measurements from multiple
155 satellites are combined to get a continuous data of atmospheric composition. These data are made by
156 assimilating the measurements from OMI (Ozone Monitoring Instrument), MLS (Microwave Limb Sounder,
157 Livesey et al., 2020), TES (Miyazaki and Bowman, 2017) and MOPITT (Measurements of Pollution in the
158 Troposphere, Deeter et al., 2003) satellite measurements. The reanalysis is made using a global CTM, and
159 an ensemble Kalman filter that optimises the concentrations of different species (Miyazaki et al., 2015). We
160 have used O_3, CH_4, NO_X, HCHO, SO_2, CO, HNO_3 and OH data from the TES reanalysis.
161
162 CAMS is the global atmospheric composition reanalysis made by the European Centre for Medium-Range
163 Weather Forecasting (ECMWF). It provides 3-dimensional time-consistent quantifications of
164 meteorological variables and concentrations of aerosols, dust and other trace gases such as OH from 2003
165 onwards. The reanalysis product offers a gridded data with a spatial resolution of 0.75°×0.75°. It has
166 relatively smaller biases with respect to the measurements, and is more reliable than that of Monitoring
167 Atmospheric Composition and Climate (MACC), the previous version of CAMS (Inness et al., 2013). All

168 variables in the CAMS reanalysis are assimilated using the IFS Cycle 42r1 4D-Var. Here, we use the monthly
169 mean OH data at the surface for the Indian and Pacific Oceans. Further information about the data is
170 provided in Inness et al. (2019).
171
172 To analyse the impact of meteorological factors on OH distribution, we have used the Tropical Rainfall
173 Measuring Mission (TRMM) daily rainfall data with a resolution of 0.25°×0.25° (TRMM, 2011; Kuttippurath
174 et al., 2021). This dataset contains the output of TRMM Algorithm 3B42 to produce the merged TRMM
175 precipitation measurements. The NOAA (National Oceanic Atmospheric Administration) Extended
176 Reconstructed Sea Surface Temperature (ERSST) Version 4 data are also considered (e.g. Huang et al., 2017;
177 Anandh et al., 2018). These monthly mean data have a spatial coverage of 2°×2°. The National Centers for
178 Environmental Prediction *(*NCEP*)* reanalysis monthly data are considered for wind, which have 17 pressure
179 levels on a horizontal resolution of 2.5°×2.5° .
180
181 The NASA-EOS Terra and Aqua spacecrafts are equipped with the MODIS sensor. Terra crosses the equator
182 southward around 10:30 local solar time (LST), while Aqua crosses northward around 13:30 LST. MODIS
183 observes the Earth in 36 channels in a spectral resolution from 0.41 to 14 µm. MODIS uses infrared bands
184 to measure cloud properties in relation to cloud top temperature and pressure. It employs visible and near
185 infrared channels to derive optical and microphysical cloud parameters (King et al., 2003). We use the
186 MODIS level 3 gridded monthly mean cloud fraction data with a spatial resolution of 1°×1° over the Indian
187 Ocean region for the year 2005. The monthly mean data are taken to estimate the seasonal distribution of
188 cloud fraction. We also use the MODIS monthly active fire product at 1 km spatial resolution. The MODIS
189 Adaptive Processing System (MODAPS) real-time active fire data are also available through Fire Information
190 for Resource Management (FIRM). These data are processed by MODAPS to the collection 5 Active fire

191 product using an enhanced contextual fire detection algorithm (Giglio et al., 2003). Here, we examine the
192 monthly mean active fire data from 2005 to 2018 in the Southeast Asian region adjacent to Indian Ocean.
193
194 In addition, we have also used the WACCM model simulations to examine the OH minimum over both
195 oceanic basins. This is a three-dimensional offline CTM with full tropospheric chemistry. The model is driven
196 by meteorological data from ECMWF reanalysis (Dee et al., 2011). The model has a horizontal resolution of
197 1°×1.25°, and the vertical co-ordinates range from the surface to 5×10^{-6} hPa. The model results are provided
198 for every 6 h. Further details about the model can be found in Wu et al. (2021) and Marsh et al. (2013).
199
200 For studying the monthly variations in the distribution of OH and other trace gases, their average for each
201 month from 2005 to 2018 is estimated. Seasonal averages are computed by finding the mean over the
202 months DJF (December, January and February) for winter, MAM (March, April and May) for spring, JJA
203 (June, July and August) for summer and SON (September, October and November) for autumn.
204
205 ## 3. Results and discussion
206 ### *3.1 The OH minimum in Indian Ocean*
207 Fig. 1 (top) shows the global surface OH distribution, and Fig. 1 (bottom) zooms into the tropical western
208 Pacific (left) where the OH hole (smaller than 1 molec./cm^3) exists and the adjacent Indian Ocean (right)
209 regions. The OH hole in the western Pacific has already been identified (Rex et al., 2014). However, similar
210 values of OH in other tropical ocean regions are not reported and are rare, although OH concentrations
211 generally decrease with latitude from tropics to the high latitudes. The OH concentrations are largest in the
212 tropical latitudes and along the shipping routes (e.g. Gopikrishnan and Kuttippurath, 2021), and they
213 gradually decrease from 30°–40° N/S to the polar regions. Since the tropical upwelling regions transport
214 atmospheric trace gases to the middle latitudes of stratosphere, the changes in OH concentrations in these

latitudes are very important. Fig. 1 (bottom, right) shows an OH minimum in Indian Ocean located at 6°–14°N and 92°–95°E, which could also be termed as a "remote" extension of the western Pacific OH hole as the Indian Ocean minimum region is in its vicinity. High reactivity of OH, about a second, is the reason for its short life span, which makes OH highly variable in time and space. Changes in the concentration of OH depend on various environmental factors such as humidity and cloudiness, intensity of incoming radiation and the presence of natural or anthropogenic pollutants (Lelieveld et al., 2004).

The monthly mean OH analysed for the past 14 years (2005–2018) is shown in Fig. 2 (top). The analysis indicates that the minimum values are spreading towards the west during the months of November, December, January and February. The minimum values are confined to a small region in this period. The OH concentration increases in the western Bay of Bengal (BoB, 8°–18°N, 76°–90°E) afterwards in March and April. The OH minimum confines to a small region in May, June, July and August, and the minimum region (6°–18°N and 80°–100°E) is surrounded by high values (e.g. 150–300×10^4 molec./cm^3). The trough of minimum is observed at a specific location and it is consistently present in all months, at 6°–14°N and 92°–95°E, and the minimum region is found around the Andaman and Nicobar Islands in the northeast Indian Ocean. We analysed another data (CAMS) for the period 2003–2018, which also displayed a very similar monthly cycle (unit of OH concentration is different here) with a region of OH minimum around 6°–18°N and 80°–100°E, as found in the TES data (Supplemental Fig. 1).

Fig. 2 (bottom) shows the monthly OH minimum in the selected latitude-longitude region (6°–18°N and 80°–100°E) averaged for the period 2005–2018. It shows two minima in a year, with the smallest values in April (15×10^4 molec./cm^3) and a secondary minimum during September–November (18×10^4 molec./cm^3), depending on year (here in November). Relatively higher values are observed in other months, about 20–40×10^4 molec./cm^3. We also analysed the CAMS data to investigate the seasonal distribution of OH

minimum, as shown in Fig. 2. The results show very similar monthly progression with the annual minimum in April (0.012 ppt) and the secondary minimum in September–November (0.015 ppt), as found in the TES reanalysis. It suggests that, although the OH minimum zone is vast and spread across hundreds of kilometers, the lowest values of OH appears in April. Henceforth, the OH minimum in Indian Ocean is seasonal and is in a relatively small region as compared to that in the western Pacific. This situation demands a detailed analysis of OH distribution in different seasons over Indian Ocean.

3.2 Seasonal Variability of OH minimum

Fig. 3 displays the minimum values of OH in the latitude region 4°–20° N for different seasons. Although the seasonal change is very small in the selected region, comparatively lower values are found in spring (MAM, about 15×10^4 molec./cm^3), consistent with our previous discussion. On the other hand, the basin-wide lowest values (< 100×10^4 molec./cm^3) are found in winter (DJF) and autumn (SON), but relatively higher values (> 200×10^4 molec./cm^3) outside the minimum region are found in summer and spring, particularly in the western BoB. We also examined the longitudinal distribution of OH in the selected region (Fig. 3, top) and it shows the smallest values (20×10^4 molec./cm^3) at 92°–95° E, which coincides the selected OH minimum region, where the seasonal differences are very small. However, beyond this minimum region (92°–95° E), the lowest OH values are found in winter and autumn. The CAMS data also yield a similar seasonal distribution of OH in BoB and in the selected region (Supplemental Fig. 2). In fact, the most critical element of OH distribution is its diurnal variation (Prinn et al., 1995). It quickly responds to solar radiation and reaches its peak concentration at noon, as the photolysis of O_3 to O(^{1}D) depends on solar radiation, and the reaction between O(^{1}D) and H_2O is the key source for OH (Rohrer and Berresheim, 2006). Additionally, the diurnal variation (TES data presented are monthly) depends on seasons, as the intensity of solar radiation at noon is stronger and duration of day is longer in summer. Accordingly, concentrations of OH are higher in summer than that in winter (Lu et al., 1991), as found in our analyses.

Fig. 4 displays OH (from CAMS), precipitation, SST, cloud cover, SO_2, CO and NO_X for different seasons in 2005. In winter, there are lower SST and less precipitation in the northern BoB, above 8° N, and are relatively higher south of that latitude. The OH production is expected to decrease under these temperature conditions and consequently, its concentration is relatively lower during this season. In April, the temperature and SST increase (highest SST in the annual cycle) and thus, higher values of OH can be found in the western BoB, but the annual minimum is observed during this period in the eastern BoB. Furthermore, the winds make a circular pattern around the minimum region north of 6^o N. In summer, heavy rainfall is observed at the east coast of BoB, about 20–30 mm. SST is also relatively high in the northern and southeastern BoB. Therefore, OH shows the highest annual concentrations over the basin in this period. The largest OH concentrations are found in the lowest precipitation regions such as 6° N along the meridional transect of BoB, and thus, the OH minimum region shrinks to its smallest in the annual cycle during this period. In autumn, SST of these regions is relatively small, providing a condition for correspondingly large OH minimum zone there.

Reaction of OH radical in cloud water play an important role in the formation of secondary aerosols. Strong seasonal cycle is observed in cloud fraction over Indian Ocean, where very high values are observed in summer and autumn (0.8–1), but relatively small fraction of clouds in winter and spring (< 0.5). Similar seasonal distribution is also observed in the region of OH minimum, where the highest cloud fractions are found in summer and autumn, and smallest in winter. However, the analysis shows that the impact of clouds on the smallest OH values in the minimum region is limited.

Since there is an active volcano in the Andaman Islands, we also examined the concentration of SO_2 in the region as it is a sink for atmospheric SO_2 (third panel from bottom). In general, relatively large concentrations are observed in the Indian coastal regions, where the seasonal highest values are observed

287 in spring (3–4 μg/m^3). The values are very small over the open ocean, but relatively high SO_2 concentrations
288 are found in the OH minimum region, which is present throughout the year. The seasonal differences are
289 very small and therefore, there are other factors controlling the OH minimum in this region. Biomass
290 burning produces a large amount of CO in earth's atmosphere, mostly within 2 km. Lu et al. (1993) showed
291 that the decrease of CO implies an increase of OH (Reaction R8). In general, the amount of CO is high during
292 winter, which decreases as summer arrives. The highest concentration of CO is observed in winter and then
293 in autumn, and the smallest in summer. Furthermore, ozone is the primary precursor of OH radical and
294 therefore, the changes in ozone decides the distribution of OH in the atmosphere. The ozone distribution
295 also follows the distribution of CO, as it shows basin-wide high concentration in winter and autumn, and
296 low values in summer and spring (Supplemental Fig. 3). The minimum ozone is also found in the same
297 region of OH minimum in spring; consistent with that found in the western Pacific (Rex et al., 2014).
298 However, there are still some other processes that could drive the seasonal OH minimum in Indian Ocean,
299 as the meteorology or ocean state are not enough to explain this. Therefore, we explore the changes in
300 tropospheric chemistry to find the additional causative factors.
301
302 Being the major oxidant in the troposphere, the distribution of OH radical is connected to several trace
303 gases in the atmosphere. We analysed the monthly average of OH and its source/sink trace gases in the
304 selected region and are displayed in Fig. 5. The OH distribution shows its highest values in summer (June,
305 July and August), which decrease gradually with time until April. The smallest values are observed in winter
306 and spring (December through April). The fire counts and CO distribution follow similar temporal
307 progression until September, as biomass burning is a major source for CO, and OH shows smaller values
308 during the periods of high CO concentrations. Similarly, one of the mechanisms by which OH is lost is its
309 reaction with NO_2 under high NO_x conditions. The formation of HNO_3 normally indicates the reaction of OH
310 with NO_2 and the loss of OH (i.e., R10); a reason for the opposite monthly distribution of NO_2 and OH here.

311 Besides, the distribution of OH radical is associated with certain other trace gases such as HONO, CH_4 and
312 HCHO, and changes in the concentration of those could also make analogous variation in OH distribution,
313 as illustrated in the figure. The trace gases that are the sink of OH show an opposite distribution to that of
314 OH, as illustrated by CH_4, CO and SO_2, but show the lowest values in April during the annual OH minimum.
315 Seasonal variability of OH depends on a number of factors, such as the changes in solar radiation and the
316 amount of water vapor, as H_2O has a major role in the production of OH radicals (e.g. see the temporal
317 distribution of H_2O in the figure). The primary production of OH by photolysis of ozone happens in the
318 presence of water vapour. In addition, photolysis of H_2O at wavelength in first continuum is an alternate
319 source for the production of OH radical (Ung and Back, 1964):

320 $H_2O + h\nu \rightarrow H + OH$ (R 11)

321 As shown by Lu et al. (1991), in an unpolluted troposphere, 50% of OH is generated by the reaction between
322 H_2O and O (^1D) as the direct source, as demonstrated in the figure.

323

324 *3.3 Inter-annual variability of OH minima*

325 Interannual variability of global OH concentration is mainly connected to the El Niño Southern Oscillation
326 (ENSO) events. Periods of La Niña are positively correlated with an increase in OH. This correlation is due
327 to the increased occurrence of lightning emission of NO_x during La Niña owing to more convective activity
328 during the period (Turner et. al., 2018). Biomass burning related CO emissions is another event, which may
329 also trigger the variability of OH in the atmosphere. Since Southeast Asia is a zone of biomass burning, the
330 interannual variability of OH can be highly influenced by these fire events. In general, biomass burning is
331 episodically restricted and it peaks during March–April in Southeast Asia (Huang et al., 2013; Kuttippurath
332 et al., 2020), as exhibited in the fire counts data in Fig. 5.

333

Fig. 6 shows the interannual variability of OH in its minimum zone for the period 2005–2018. The spatial variation of OH (averaged values are shown in the top panel and minimum values in the second panel from the top; averaged over 90°–98°E) for different years are depicted. The black contours indicate 20×10^4 molec./cm^3. The OH climatology over the region shows a consistent pattern of OH minimum in Indian Ocean. The seasonal minimum of OH in spring is clearly visible with concentrations of about 15×10^4 molec./cm^3 between 8° and 14° N, and the lowest around 12° N. On the other hand, high OH concentrations are observed at 5°–8° N and north of 14° N (> 200×10^4 molec./cm^3). Since this is the monthly climatology, the interannual changes are hardly visible. Therefore, we also examined the minimum values of each month (second panel from the top). The analyses show the lowest OH concentrations between 10° and 13° N, and are blow 20×10^4 molec./cm^3. The latitude regions north and south of these seasonal minima show OH values of about 50–100×10^4 molec./cm^3. The highest OH values are observed beyond these minima zones, i. e. at 7°–5° N and 17°–19°, about 200×10^4 molec./cm^3 or higher. The inter-annual changes are very large and explicit in these analyses. For instance, the minimum values are found in relatively smaller regions in 2005, 2011 and 2012.

To diagnose the characteristics of minimum region and its year-to-year changes, we found the average values in each month for the minimum region and are shown in the bottom four panels. The lowest minimum in the TES data is observed in 2009 and 2016 (around 60×10^4 molec./cm^3), and the yearly minima are in the range of 40–60 $\times10^4$ molec./cm^3. In general, the minimum peaks are found in spring. CO emitted from biomass burning might have caused this variability, as this is the peak biomass burning season in South Asia (Huang et al., 2013). Conversely, high values are observed in December and January, and even the minimum trough was absent in 2010. As mentioned earlier, the inter-annual variability of ozone and CO is highly connected to ENSO events (e.g. Xue et al., 2021). Therefore, there is a strong relationship between ENSO events and OH minimum. In most years, we find higher values of OH during La Niña periods. For

instance, the year 2010 had a strong La Niña, which could be the reason for the absence of OH minimum in that year. Since H_2O is a source for OH, its monthly and yearly distributions are in agreement with those of H_2O. Conversely, as CO, SO_2 and CH_4 are known to be the sink of OH, their monthly and yearly distributions are opposite to those of OH, except in the annual minimum period of April. These analyses also expose relatively high values of OH from 2015 onwards, which can be due to the slight reduction in its sink (three bottom panels).

3.4 Comparison with the western Pacific OH minimum

An OH minimum or OH hole has already been reported in the tropical western Pacific. Very small values of ozone in this region (i.e. clean air) is the main reason for this (Rex et al., 2014). Tropical pacific is the major source/pathway of trace gases to the stratosphere and thus, the region has a great significance in terms of atmospheric composition. Here, we compare the OH hole in the Pacific with the Indian Ocean OH minimum, as it is adjacent to the Pacific Ocean that plays a key role in stratospheric and tropospheric exchange of trace gases. Fig. 7 shows the OH minimum values in Indian and Pacific Oceans for each month from 2005 to 2018. It is evident that the western Pacific OH minimum is small enough to call a "hole" and is present throughout the year. In contrast, the OH minimum in Indian Ocean is seasonal, where the lowest values appear in April. As mentioned, the lowest OH minimum in Indian Ocean is about $10–20\times10^5$ molec./cm^3, depending on month and year. The CAMS data (dashed lines) replicate the monthly and interannual variability of OH minimum in both oceanic regions, as demonstrated with the TES data.

3.5 Modelled OH minimum

To examine the existence of OH minimum, we simulated the distribution of OH in the Indian and Pacific Oceans using the WACCM model (Fig. 8). The model reproduces the general features of OH distribution across the latitudes, with the highest concentrations in the tropics, which decreases with latitude towards

382 the poles. The model shows the highest values in summer (June–September) and the smallest in autumn,
383 winter and spring (in March), as for the TES data. Therefore, the seasonal cycle shows the highest values in
384 summer and spring, and the smallest in winter and autumn, as found with the TES data outside the OH
385 minimum region (Supplemental Fig. 4). However, the model hardly finds the seasonal minimum in the
386 selected region, where the annual minimum is as it is found for the other regions over the basin. The
387 simulations for different years and for the western Pacific (Supplemental Fig. 5) indicate that the model
388 struggles to capture the OH hole, although there is a seasonal minimum in winter as over Indian Ocean.
389 Horizontal resolution of the model can be one of the primary reasons for this difference, although different
390 chemical reactions, representation of photolysis of O_3, and the modelled results of ozone and CO play a
391 decisive role in simulating OH values by the model (e.g. Nicely et al., 2017). Since OH minima or hole are
392 extreme values, simulating this atmospheric chemistry would be a great challenge for any CTM. Therefore,
393 dedicated model studies are required to infer the simulations of such extreme cases. This is a future study
394 as the model sensitivity assessment is beyond the scope of this work.
395
396 *3.6 Limitation of the study*
397 This study is based on the renalysed data as there are no direct measurements from *in situ* instruments or
398 satellites in the region concerned. Since these data are heavily weighted by the simulations from a model
399 that used for making the reanalysis, our assessment with the same also has this particular limitation,
400 because modelling of OH is challenging and many uncertainties are still there (e.g. Nicely et al., 2018). This
401 is the reason that we used two different reanalysed data sets here. In addition, we have also used model
402 results for examining the representation of OH minimum in CTMs. The region in which the OH minimum
403 has found is around the Andaman and Nicobar Islands and there is an active volcano on the island. This
404 suggests that the island land mass also has a role in the particular distribution OH there. Our study reiterate

the need of more OH and related trace gas measurements in the region for a solid conclusion about the OH minimum over Indian Ocean.

4. Conclusions

The OH distribution over Indian Ocean exhibits two minima, in spring and autumn, as assessed from the TES and CAMS renalyses. The spring concentrations reach to 15×10^4 molec./cm^3 and slightly higher in autumn (SON). The minimum region is found near the Andaman and Nicobar Islands in Indian Ocean, where it houses an active volcano. The concentration of SO_2 is relatively higher there, which is also the only region over BoB with high SO_2 concentrations, except near the coasts. Since SO_2 is one of the sinks of OH, this could be a reason for the OH minimum there. In general, the sink trace gases (e.g. CO, SO_2 and CH_4) show an opposite temporal distribution to that of OH in the minimum region. The minimum troughs were present in all years, except in the strong La Niña year 2010. The OH distribution shows an anti-correlation with ENSO events, and therefore, relatively higher OH concentrations are found during the La Niña years. The analyses also reveal that the biomass burning and CO distribution have significant influence on the distribution of OH minimum, as the OH chemistry is closely linked to the changes in O_3, CO and HNO_3. The model struggles to capture the OH minimum in both oceans, which demand more dedicated studies with high resolution simulations. In brief, the OH minimum in the western Pacific Ocean is owing to its clean air there, but it is very likely due to the polluted air over Indian Ocean. As OH has the control on the cleansing capacity of atmosphere, its changes will affect air quality and troposphere-stratosphere exchange, which in turn, would affect public and ecosystem health, and climate of the region. Therefore, this study suggests a continuous monitoring of atmospheric OH over Indian Ocean.

Credit authorship contribution statement

JK: Conceptualization, Methodology, Supervision, Visualization, Writing-original draft, review & editing of the original draft, **AD, SR, WF:** Methodology, Data Analysis, Visualization, Writing - original draft

Acknowledgement

We thank the Director, Indian Institute of Technology Kharagpur (IIT Kgp), Chairman of CORAL IIT Kgp and the Ministry of Education (MoE) for facilitating the study. We thank Indian Institute of Technology Kharagpur, Ministry of Education (MoE), Naval Research Board (OEP), Defence Research Development Organisation, National Centre for Ocean Information Services (INCOIS) Hyderabad and Ministry of Earth Science (MoES) for facilitating and partly funding the study. JK acknowledges his gratitude to V K Patel and G S Gopikrishnan for their help with the data analysis. We thank the scientific organisations and scientists who made available the TES and CAMS reanalyses, TRMM precipitation, ERSST and ENSO index data for this study. The TMPA data were provided by the NASA/Goddard Space Flight Center's Mesoscale Atmospheric Processes Laboratory and PPS, which develop and compute the TMPA as a contribution to TRMM.

Data availability

The data used in this study are publicly available.

TES chemical reanalyses : https://tes.jpl.nasa.gov/chemical-reanalysis/,

TRMM on http: // mirador.gsfc.nasa.gov/cgibin/mirador/

ERSST data: https://www1.ncdc.noaa.gov/pub/data/cmb/ersst/v5/netcdf/.

MERRA 2 data are available on: https://giovanni.gsfc.nasa.gov/giovanni/

The CAMS data are available on: https://ads.atmosphere.copernicus.eu/#!/search?text=reanalysis

MODIS fire count data: https://firms.modaps.eosdis.nasa.gov/active_fire/

Additional Information

Declaration

The authors confirm that there are no known conflicts of interest associated with this article.

Competing Interest

The authors declare no competing interest.

References

Anandh, T.S., Das, B.K., Kumar, B., Kuttippurath, J., Chakraborty, A., 2018. Analyses of the oceanic heat content during 1980–2014 and satellite-era cyclones over Bay of Bengal. Int. J. Climatol. 38, 5619–5632. https://doi.org/10.1002/JOC.5767

Cady-Pereira, K.E., Payne, V.H., Neu, J.L., Bowman, K.W., Miyazaki, K., Marais, E.A., Kulawik, S., Tzompa-Sosa, Z.A., Hegarty, J.D., 2017. Seasonal and spatial changes in trace gases over megacities from Aura TES observations: Two case studies. Atmos. Chem. Phys. 17, 9379–9398. https://doi.org/10.5194/ACP-17-9379-2017

Dee, D.P., Uppala, S.M., Simmons, A.J., Berrisford, P., Poli, P., Kobayashi, S., Andrae, U., Balmaseda, M.A., Balsamo, G., Bauer, P., Bechtold, P., Beljaars, A.C.M., van de Berg, L., Bidlot, J., Bormann, N., Delsol, C., Dragani, R., Fuentes, M., Geer, A.J., Haimberger, L., Healy, S.B., Hersbach, H., Hólm, E. V., Isaksen, L., Kållberg, P., Köhler, M., Matricardi, M., Mcnally, A.P., Monge-Sanz, B.M., Morcrette, J.J., Park, B.K., Peubey, C., de Rosnay, P., Tavolato, C., Thépaut, J.N., Vitart, F., 2011. The ERA-Interim reanalysis: configuration and performance of the data assimilation system. Q. J. R. Meteorol. Soc. 137, 553–597. https://doi.org/10.1002/QJ.828

Deeter, M.N., Emmons, L.K., Francis, G.L., Edwards, D.P., Gille, J.C., Warner, J.X., Khattatov, B., Ziskin, D.,

473 Lamarque, J.F., Ho, S.P., Yudin, V., Attié, J.L., Packman, D., Chen, J., Mao, D., Drummond, J.R., 2003.
474 Operational carbon monoxide retrieval algorithm and selected results for the MOPITT instrument. J.
475 Geophys. Res. Atmos. 108, 4399. https://doi.org/10.1029/2002JD003186

476 Elshorbany, Y., Barnes, I., Becker, K.H., Kleffmann, J., Wiesen, P., 2010. Sources and cycling of
477 tropospheric hydroxyl radicals - An overview. Zeitschrift fur Phys. Chemie 224, 967–987.
478 https://doi.org/10.1524/ZPCH.2010.6136/MACHINEREADABLECITATION/RIS

479 Giglio, L., Descloitres, J., Justice, C.O., Kaufman, Y.J., 2003. An Enhanced Contextual Fire Detection
480 Algorithm for MODIS. Remote Sens. Environ. 87, 273–282. https://doi.org/10.1016/S0034-
481 4257(03)00184-6

482 Gopikrishnan, G.S., Kuttippurath, J., 2021. A decade of satellite observations reveal significant increase in
483 atmospheric formaldehyde from shipping in Indian Ocean. Atmos. Environ. 246, 118095.
484 https://doi.org/10.1016/J.ATMOSENV.2020.118095

485 Huang, B., Thorne, P.W., Banzon, V.F., Boyer, T., Chepurin, G., Lawrimore, J.H., Menne, M.J., Smith, T.M.,
486 Vose, R.S., Zhang, H.M., 2017. Extended Reconstructed Sea Surface Temperature, Version 5
487 (ERSSTv5): Upgrades, Validations, and Intercomparisons. J. Clim. 30, 8179–8205.
488 https://doi.org/10.1175/JCLI-D-16-0836.1

489 Huang, K., Fu, J.S., Hsu, N.C., Gao, Y., Dong, X., Tsay, S.C., Lam, Y.F., 2013. Impact assessment of biomass
490 burning on air quality in Southeast and East Asia during BASE-ASIA. Atmos. Environ. 78, 291–302.
491 https://doi.org/10.1016/J.ATMOSENV.2012.03.048

492 Inness, A., Baier, F., Benedetti, and the MACC team., 2013. The MACC reanalysis: an 8 yr data set of
493 atmospheric composition. Atmos. Chem. Phys. 13, 4073–4109, https://doi.org/10.5194/acp-13-
494 4073-2013.

Inness, A., Ades, M., Agustí-Panareda, A., Barr, J., Benedictow, A., Blechschmidt, A.M., Jose Dominguez, J., Engelen, R., Eskes, H., Flemming, J., Huijnen, V., Jones, L., Kipling, Z., Massart, S., Parrington, M., Peuch, V.H., Razinger, M., Remy, S., Schulz, M., Suttie, M., 2019. The CAMS reanalysis of atmospheric composition. Atmos. Chem. Phys. 19, 3515–3556. https://doi.org/10.5194/ACP-19-3515-2019

King, M.D., Menzel, W.P., Kaufman, Y.J., Tanré, D., Gao, B.C., Platnick, S., Ackerman, S.A., Remer, L.A., Pincus, R., Hubanks, P.A., 2003. Cloud and aerosol properties, precipitable water, and profiles of temperature and water vapor from MODIS. IEEE Trans. Geosci. Remote Sens. 41, 442–456. https://doi.org/10.1109/TGRS.2002.808226

Kuttippurath, J., Murasingh, S., Stott, P.A., Balan Sarojini, B., Jha, M.K., Kumar, P., Nair, P.J., Varikoden, H., Raj, S., Francis, P.A., Pandey, P.C., 2021. Observed rainfall changes in the past century (1901–2019) over the wettest place on Earth. Environ. Res. Lett. 16, 024018. https://doi.org/10.1088/1748-9326/ABCF78

Kuttippurath, J., Singh, A., Dash, S.P., Mallick, N., Clerbaux, C., Van Damme, M., Clarisse, L., Coheur, P.F., Raj, S., Abbhishek, K., Varikoden, H., 2020. Record high levels of atmospheric ammonia over India: Spatial and temporal analyses. Sci. Total Environ. 740, 139986. https://doi.org/10.1016/j.scitotenv.2020.139986

Lelieveld, J., Dentener, F.J., Peters, W., Krol, M.C., 2004. On the role of hydroxyl radicals in the self-cleansing capacity of the troposphere. Atmos. Chem. Phys. 4, 2337–2344. https://doi.org/10.5194/ACP-4-2337-2004

Lelieveld, J., Gromov, S., Pozzer, A., Taraborrelli, D., 2016. Global tropospheric hydroxyl distribution, budget and reactivity. Atmos. Chem. Phys. 16, 12477–12493. https://doi.org/10.5194/ACP-16-12477-2016

Levy, H., 1971. Normal Atmosphere: Large Radical and Formaldehyde Concentrations Predicted. Science (80-.). 173, 141–143. https://doi.org/10.1126/SCIENCE.173.3992.141

Livesey, N. J. et al.: EOS MLS Version 4.2x Level 2 data quality and description document (Revision E), 2020. Tech. Rep., Jet Propulsion Laboratory, available at: https://mls.jpl.nasa.gov/eos-aura-mls/data-documentation (last access: 29 September, 2021), (data available at: https://disc.gsfc.nasa.gov, last access: 29 September 2021).

Lu, Y., Khalil, M.A.K., 1993. Methane and carbon monoxide in OH chemistry: The effects of feedbacks and reservoirs generated by the reactive products. Chemosphere 26, 641–655. https://doi.org/10.1016/0045-6535(93)90450-J

Lu, Y., Khalil, M.A.K., 1991. Tropospheric OH: model calculations of spatial, temporal, and secular variations. Chemosphere 23, 397–444. https://doi.org/10.1016/0045-6535(91)90194-I

Manning, M.R., Lowe, D.C., Moss, R.C., Bodeker, G.E., Allan, W., 2005. Short-term variations in the oxidizing power of the atmosphere. Nat. 2005 4367053 436, 1001–1004. https://doi.org/10.1038/nature03900.

Marsh, D., Mills, M., Kinnison, D. E., & Lamarque, J. -F., 2013. Climate change from 1850 to 2005 simulated in CESM1(WACCM). Journal Of Climate 26, 7372-7391. doi:10.1175/JCLI-D-12-00558.1

Miyazaki, K., Bowman, K., 2017. Evaluation of ACCMIP ozone simulations and ozonesonde sampling biases using a satellite-based multi-constituent chemical reanalysis. Atmos. Chem. Phys. 17, 8285–8312. https://doi.org/10.5194/ACP-17-8285-2017

Miyazaki, K., Eskes, H.J., Sudo, K., 2015. A tropospheric chemistry reanalysis for the years 2005-2012 based on an assimilation of OMI, MLS, TES, and MOPITT satellite data. Atmos. Chem. Phys. 15, 8315–8348. https://doi.org/10.5194/ACP-15-8315-2015

Nicely, J. M., Salawitch, R. J., Canty, T., Anderson, D. C., Arnold, S. R., Chipperfield, M. P., et al., 2017. Quantifying the causes of differences in tropospheric OH within global models. Journal of Geophysical Research: Atmospheres, 122, 1983–2007. https://doi.org/10.1002/2016JD026239.

Nicely, J. M., Canty, T. P., Manyin, M., Oman, L. D., Salawitch, R. J., Steenrod, S. D., et al. (2018). Changes in global tropospheric OH expected as a result of climate change over the last several decades. Journal of Geophysical Research: Atmospheres, 123, 10,774–10,795. https://doi.org/10.1029/2018JD028388

Prinn, R.G., Weiss, R.F., Miller, B.R., Huang, J., Alyea, F.N., Cunnold, D.M., Fraser, P.J., Hartley, D.E., Simmonds, P.G., 1995. Atmospheric Trends and Lifetime of CH3CCI3 and Global OH Concentrations. Science (80-.). 269, 187–192. https://doi.org/10.1126/SCIENCE.269.5221.187

Rex, M., Wohltmann, I., Ridder, T., Lehmann, R., Rosenlof, K., Wennberg, P., Weisenstein, D., Notholt, J., Krüger, K., Mohr, V., Tegtmeier, S., 2014. A tropical West Pacific OH minimum and implications for stratospheric composition. Atmos. Chem. Phys. 14, 4827–4841. https://doi.org/10.5194/ACP-14-4827-2014

Rohrer, F., Berresheim, H., 2006. Strong correlation between levels of tropospheric hydroxyl radicals and solar ultraviolet radiation. Nat. 2006 4427099 442, 184–187. https://doi.org/10.1038/nature04924

Tropical Rainfall Measuring Mission (TRMM) (2011), TRMM (TMPA) Rainfall Estimate L3 3 hour 0.25 degree x 0.25 degree V7, Greenbelt, MD, Goddard Earth Sciences Data and Information Services Center (GES DISC), Accessed: [Data Access Date], 10.5067/TRMM/TMPA/3H/7

Turner, A.J., Fung, I., Naik, V., Horowitz, L.W., Cohen, R.C., 2018. Modulation of hydroxyl variability by ENSO in the absence of external forcing. Proc. Natl. Acad. Sci. U. S. A. 115, 8931–8936. https://doi.org/10.1073/PNAS.1807532115/SUPPL_FILE/PNAS.1807532115.SAPP.PDF

562 Ung, A.Y.-M., Back, R.A., 1964. The photolysis of water vapor and reactions of hydroxyl radicals. Can. J.
563 Chem. 42, 753–763. https://doi.org/10.1139/V64-114

564 Vogel, B., Vogel, H., Kleffmann, J., Kurtenbach, R., 2003. Measured and simulated vertical profiles of
565 nitrous acid—Part II. Model simulations and indications for a photolytic source. Atmos. Environ. 37,
566 2957–2966. https://doi.org/10.1016/S1352-2310(03)00243-7

567 Wolfe, Glenn M., Nicely, J.M., Clair, J.M.S., Hanisco, T.F., Liao, J., Oman, L.D., Brune, W.B., Miller, D.,
568 Thames, A., Abad, G.G., Ryerson, T.B., Thompson, C.R., Peischl, J., McCain, K., Sweeney, C.,
569 Wennberg, P.O., Kim, M., Crounse, J.D., Hall, S.R., Ullmann, K., Diskin, G., Bui, P., Chang, C., Dean-
570 Day, J., 2019a. Mapping hydroxyl variability throughout the global remote troposphere via synthesis
571 of airborne and satellite formaldehyde observations. Proc. Natl. Acad. Sci. U. S. A. 166, 11171–
572 11180. https://doi.org/10.1073/PNAS.1821661116/SUPPL_FILE/PNAS.1821661116.SAPP.PDF

573 Wolfe, G M, Nicely, J.M., St.Clair, J.M., Hanisco, T.F., Liao, J., Oman, L., Brune, W.H., Miller, D.O., Thames,
574 A.B., Abad, G.G., Ryerson, T.B., Peischl, J., Mccain, K., Sweeney, C., Wennberg, P., Kim, M.J., Crounse,
575 J.D., Hall, S.R., Ullmann, K., Diskin, G.S., Bui, T.P., Chang, C.S., Dean-Day, J.M., 2019b. ATom: Column-
576 Integrated Densities of Hydroxyl and Formaldehyde in Remote Troposphere.
577 https://doi.org/10.3334/ORNLDAAC/1669.

578 Wu J, Feng W, Liu H-L, Xue X, Marsh DR, Plane J., 2021. Self-consistent Global Transport of Metallic Ions
579 with WACCM-X. Atmospheric Chemistry and Physics. 21, pp. 15619-15630

580 Xue, L., Ding, A., Cooper, O., Huang, X., Wang, W., Zhou, D., Wu, Z., McClure-Begley, A., Petropavlovskikh,
581 I., Andreae, M.O., Fu, C., 2021. ENSO and Southeast Asian biomass burning modulate subtropical
582 trans-Pacific ozone transport. Natl. Sci. Rev. 8. https://doi.org/10.1093/NSR/NWAA132

583

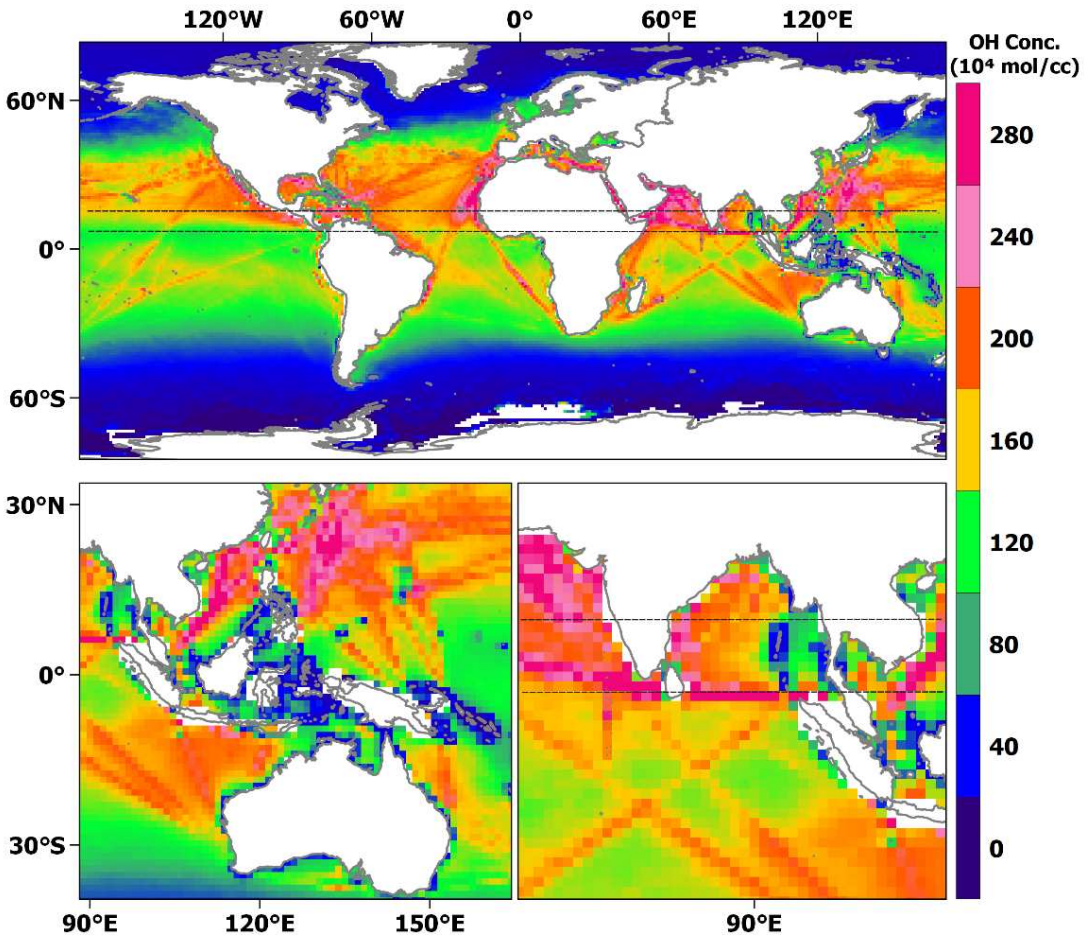

Fig. 1. The upper panel shows the global surface OH concentration for May 2009. The bottom panels show the surface OH distribution over the western Pacific (left) and Indian (right) Oceans for May 2009. The horizontal dotted lines demarcate the region of OH minimum in Indian Ocean and the lines extend across the longitudes to examine any such areas in other oceanic regions.

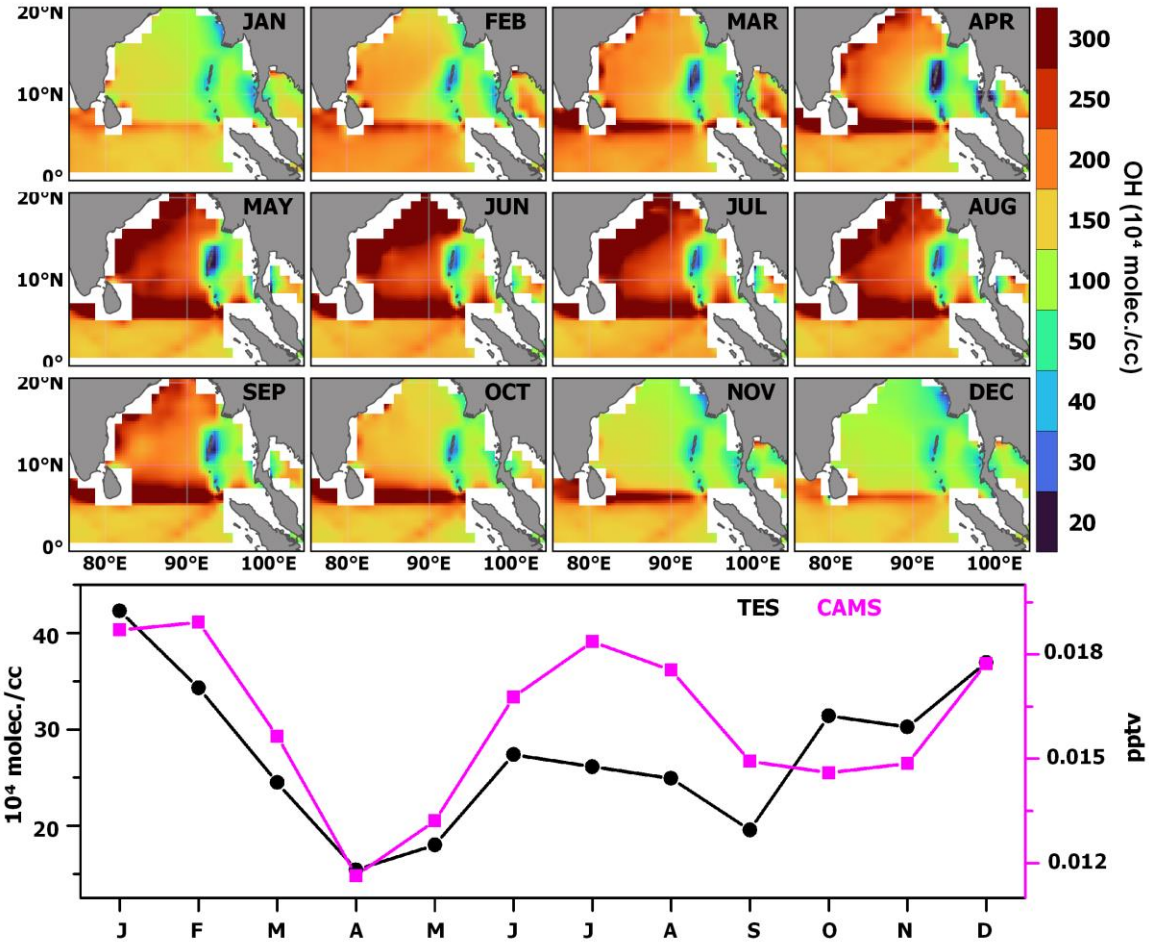

595

596 **Fig. 2.** The monthly distribution of surface OH over the eastern north Indian Ocean for the period 2005–
597 2018. The regional average of monthly mean surface OH for the minimum region is illustrated in the bottom
598 panel. The months are represented by their first three letters in the top panel (e.g. JAN is January) and by
599 their first letter on the x-axis of bottom panel (e.g. J is for January and D is for December).

600

601

602

603

604

605

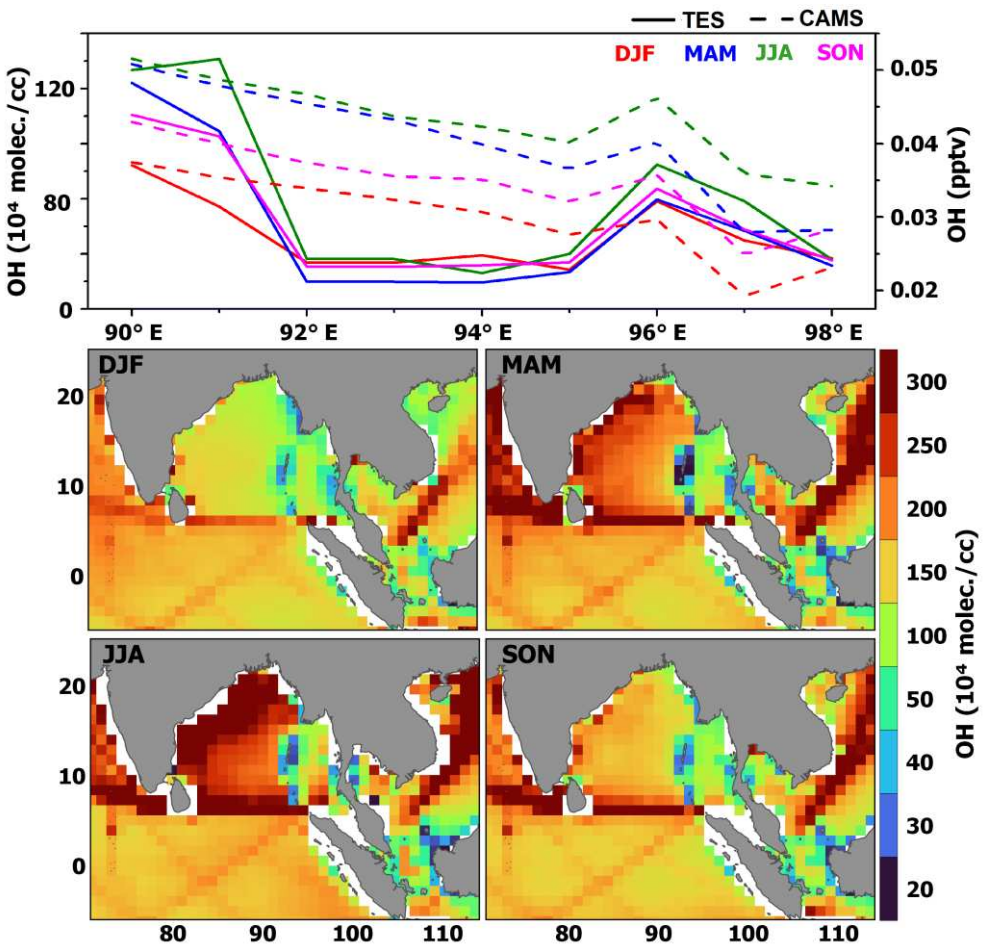

606

607 Fig. 3. Top: distribution of surface OH averaged over the latitude band 4°–20° N (i.e. minimum region) for
608 different seasons. Bottom: distribution of surface OH averaged for each season for the period 2005–2018
609 in the eastern north Indian Ocean. The seasons are defined as winter (DJF), spring (MAM), summer (JJA)
610 and autumn (SON).

611

612

613

614

615

616

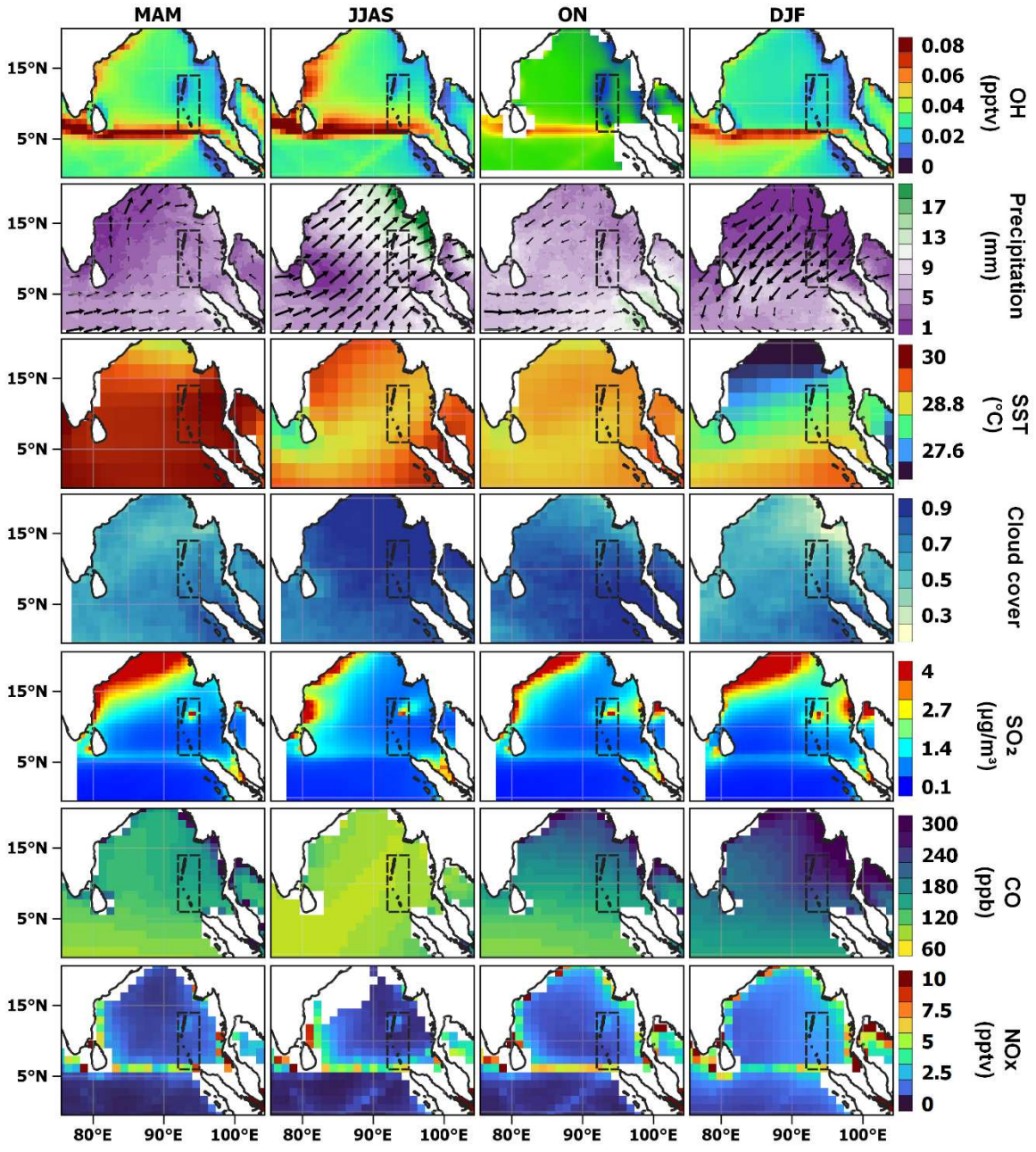

Fig. 4. Surface concentration of OH from CAMS, precipitation (winds overlaid), SST, cloud cover, SO_2, CO and NO_X for different seasons in eastern north Indian Ocean for the year 2005. The northern hemispheric seasons are defined as winter (DJF), spring (MAM), summer (JJAS) and autumn (ON). Here, summer season includes the month of September to examine the monsoon precipitation.

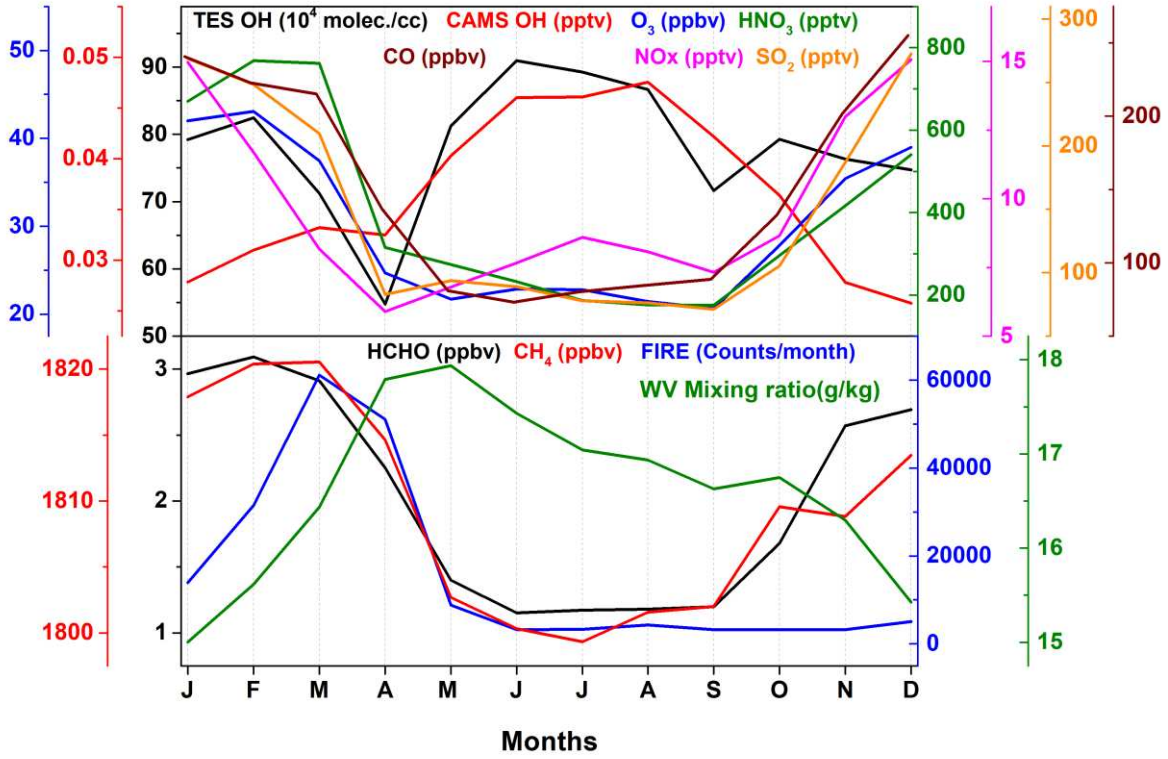

624

625 Fig. 5. Monthly distribution of surface OH and other trace gases averaged over the OH minimum region

626 (6°–14°N and 92°–95°E) for the period 2005–2018. The months are represented by their first letter on the

627 x-axis (e.g. J is for January and D is for December).

628

629

630

631

632

633

634

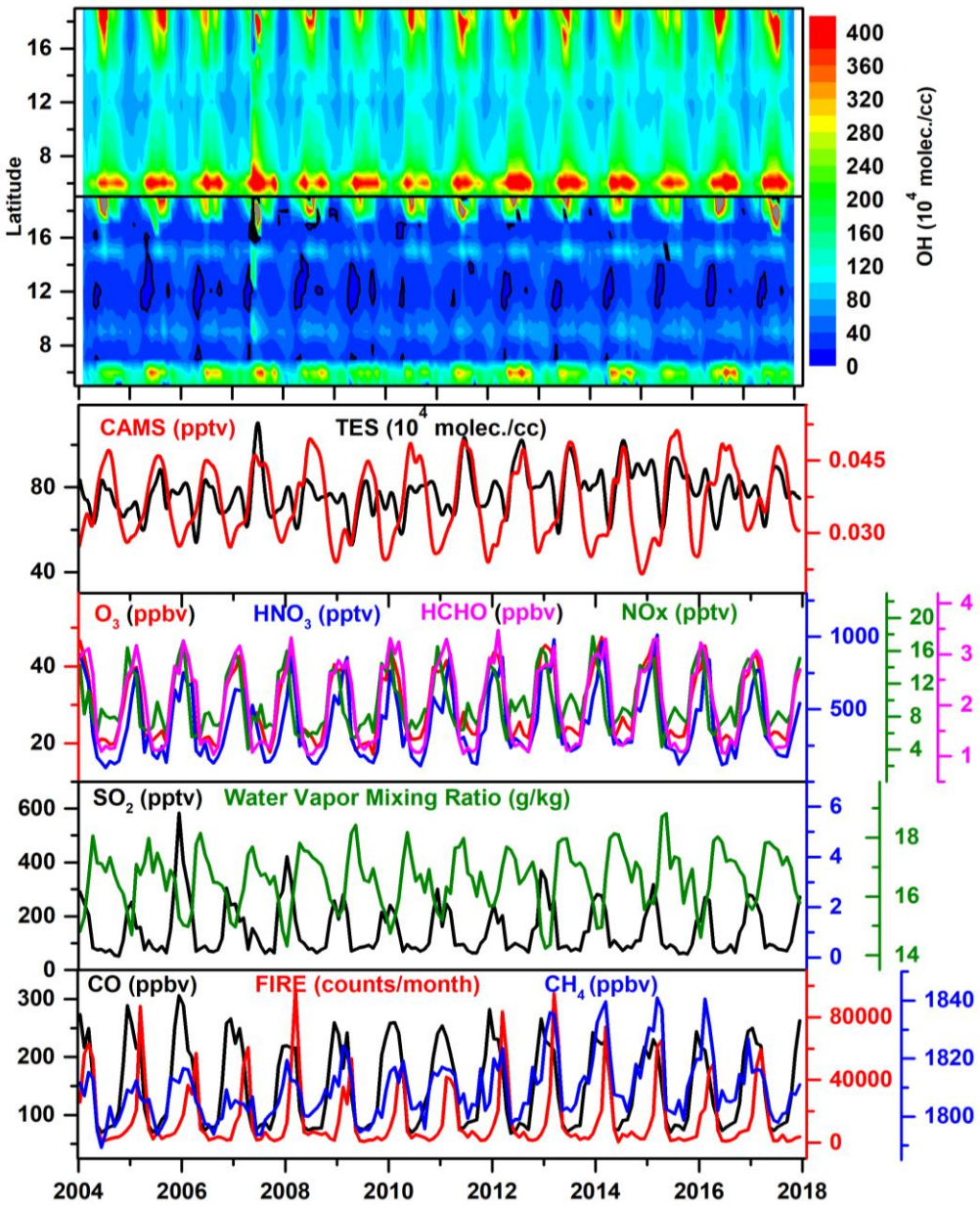

635

636 **Fig. 6**. Surface OH concentration averaged over the longitudes 90°–98°E for the period 2005–2018. Here,
637 the top panel shows the average of surface OH (top) and the second panel from top shows the minimum
638 of surface OH in the selected region. The bottom panels show the concentrations of mean surface OH
639 estimated from the TES and CAMS reanalysis data (third panel from top), and different trace gases averaged
640 over the minimum region for the study period. All data are monthly averaged.

641

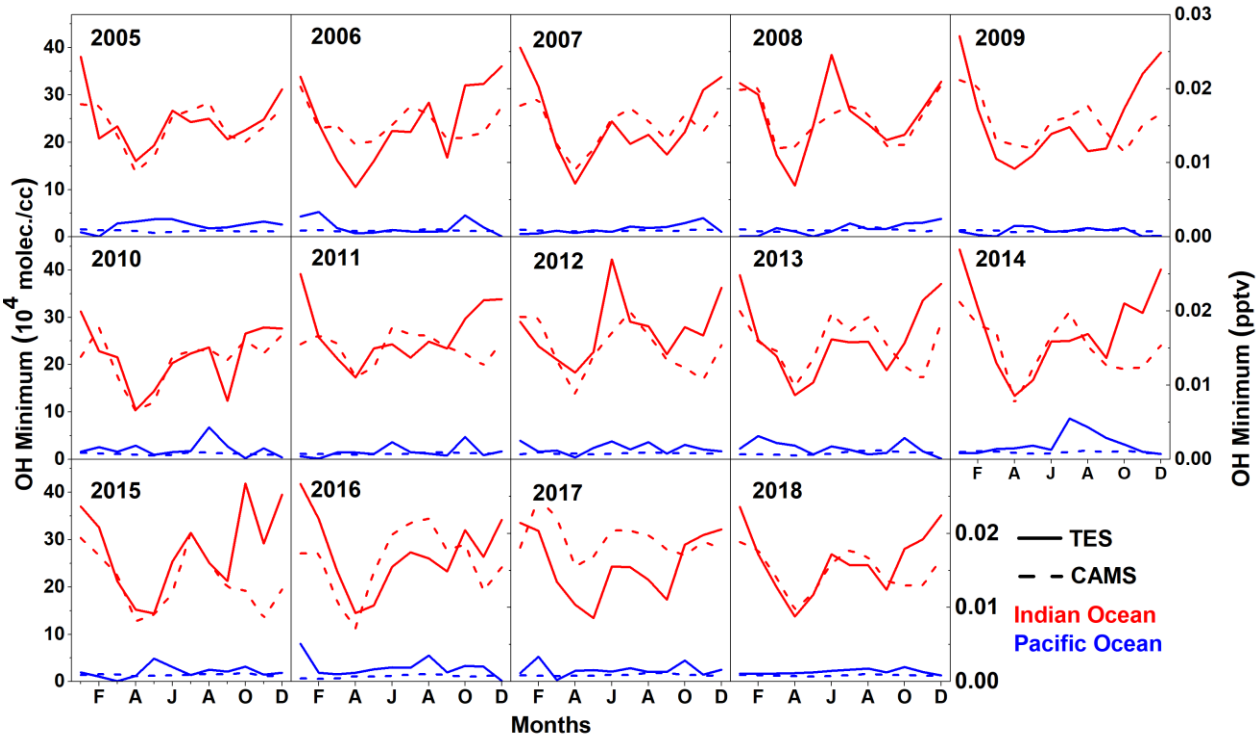

642

643 **Fig. 7.** The OH minima at the surface of Pacific and Indian Oceans averaged for each month and year.

644 Alternate months are marked on the x-axis (e.g. February is F, April is A and December is D).

645

646

647

648

649

650

651

652

653

654

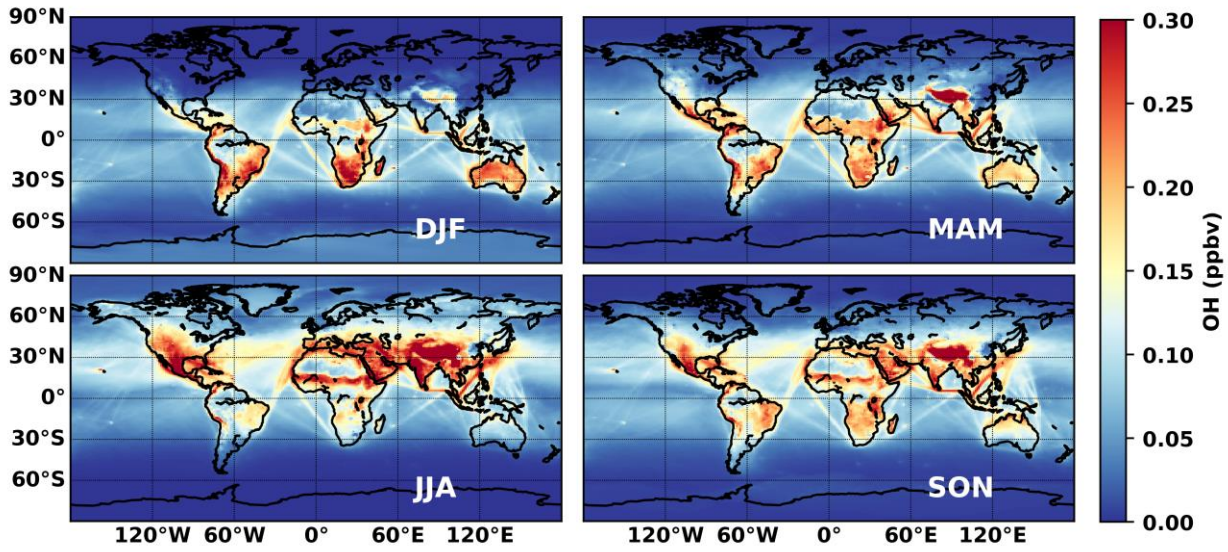

655

656 **Fig. 8.** Surface OH values simulated by the WACCM model for different seasons of 2005. The seasons are

657 defined as winter (DJF), spring (MAM), summer (JJA) and autumn (SON).

658

659 2REV/JK/V04/30112022/0114AM